Inorganic Chemistry

Article

pubs.acs.org/IC

Nonstoichiometric Perovskite $CaMnO_{3-\delta}$ for Oxygen Electrocatalysis with High Activity

Jing Du,[†] Tianran Zhang,[†] Fangyi Cheng,[†] Wangsheng Chu,[‡] Ziyu Wu,[‡] and Jun Chen*[,†]

[†]Key Laboratory of Advanced Energy Materials Chemistry (Ministry of Education), Collaborative Innovation Center of Chemical Science and Engineering (Tianjin), College of Chemistry, Nankai University, Tianjin 300071, China

[‡]National Synchrotron Radiation Laboratory, University of Science and Technology of China, Hefei 230029, China

S *Supporting Information*

ABSTRACT: Perovskite oxides offer efficient and cheap electrocatalysts for both oxygen reduction reactions and oxygen evolution reactions (ORR/OER) in diverse oxygen-based electrochemical technologies. In this study, we report a facile strategy to enhance the electrocatalytic activity of $CaMnO_3$ by introducing oxygen defects. The nonstoichiometric $CaMnO_{3-\delta}$ ($0 < \delta \leq 0.5$) was prepared through thermal reduction of pristine perovskite microspheres and nanoparticles, which were synthesized from thermal-decomposition of carbonate precursors and the Pechini route, respectively. The as-prepared samples were analyzed by chemical titration, structural refinement, thermogravimetric analysis, and energy spectrometry. In 0.1 M KOH aqueous solution, the nonstoichiometric $CaMnO_{3-\delta}$ with δ near 0.25 and an average Mn valence close to 3.5 exhibited the highest ORR activity (36.7 A g^{-1} at 0.70 V vs RHE, with onset potential of 0.96 V), which is comparable to that of benchmark Pt/C. Density functional theory (DFT) studies and electrical conductivity measurement revealed that the enhanced ORR kinetics is due to facilitated oxygen activation and improved electrical properties. Besides high activity, the nonstoichiometric perovskite oxides showed respectable catalytic stability. Furthermore, the moderate oxygen-defective $CaMnO_{3-\delta}$ ($\delta \approx 0.25$) favored the OER because of the improved electrical conductivity. This study makes nonstoichiometric $CaMnO_{3-\delta}$ a promising active, inexpensive bifunctional catalytic material for reversible ORR and OER.

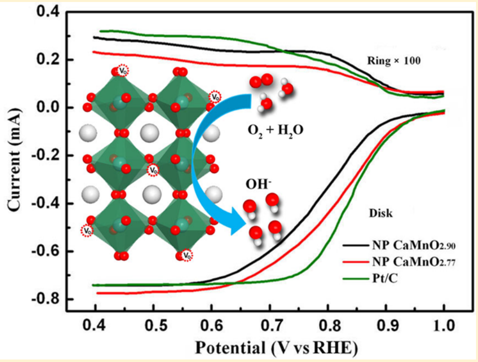

■ INTRODUCTION

The catalysts for oxygen reduction reaction (ORR) and oxygen evolution reaction (OER) play a key role in the devices of electrochemical energy storage and conversion including metal-air batteries and fuel cells.[1,2] Pt and Pt-based alloys show high performance of ORR, while RuO_2 and IrO_2 display high catalysis of OER. Although these noble metal-based catalysts exhibit the best overall electrocatalytic performance,[3] the prohibitive cost and scarcity severely preclude their widespread applicability. Extensive efforts have been dedicated to exploiting transition-metal oxides for catalyzing ORR ($O_2 + H_2O + 4e^- \rightarrow 4OH^-$) and the reverse reaction of ORR.[4−9] Among various catalysts, manganese oxides have attracted particular interest because of their high natural abundance, low cost, and environmental friendiness.[10−17] However, manganese oxides occur in a variety of polymorphs with variable Mn valences, making it elusive in deciphering the catalytic sites and indentifying the activity-determining parameters.[5,15,18,19] Furthermore, unmodified and bulk manganese oxides, particularly in the simple binary oxide forms, normally possess relatively low electrical conductivity and poor chemical/structural stability under severe aging conditions.[12,20] Thus, elucidating the structure−activity correlation and improving the electrocatalytic performance of manganese oxides are necessary to make full use of such promising electrocatalysts.

Composite metal-oxides compounds, which incorporate two or more metallic elements into one oxide framework, have been the focus of tremendous studies in the context of oxygen electrocatalysis.[21−25] The multiple oxidation states and variable crystal structures of composite oxides give rise to rich materials properties and redox electrochemistry, entailing challenges yet opportunities to screen superior catalysts. In nature, the Mn−Ca-oxo oxygen-evolving complex (OEC) in photosystem II (PS II) catalyzes the light-driven water oxidation through different redox states of Mn.[26−28] Inspiration from the biological OEC active sites has triggered substantial interest in calcium−manganese composite oxides for the oxygen electrode catalysts in previous report.[29] Our motivation is the structural and compositional flexibility of the perovskite family with general formula of ABO_3. In this family, the metal ions accommodate a variable oxidation state, and the anionic sublattice bears a large amount of vacancies, enabling researchers to explore their physicochemical and catalytic properties.[21,30] Furthermore, the nonstoichiometry of transition metal oxides has been demonstrated to exert a prominent effect on the performance of different electrochemical systems such as lithium-ion batteries and fuel cells.[22,31] The nonstoichiometry can

Received: May 13, 2014
Published: August 18, 2014

dx.doi.org/10.1021/ic501631h | *Inorg. Chem.* 2014, 53, 9106−9114

contribute to an improvement in the intrinsic electrical conductivity. However, reports on the electrocatalytic behavior of nonstoichiometric orthorhombic Ca−Mn−O perovskites in alkaline media are still limited.

In this work, we prepared nonstoichiometric perovskite-type calcium−manganese oxides ($CaMnO_{3-\delta}$, $0 < \delta \leq 0.5$) and investigated the performance of nonstoichiometric $CaMnO_3$ for the bifunctional electrocatalysis of ORR and OER. The oxide nonstoichiometry was adjusted via controllable thermal reduction of pristine perovskite microspheres and nanoparticles synthesized from thermal decomposition of carbonate precursors and the Pechini route, respectively. Electrochemical investigations revealed that the catalytic activity exhibits a strong dependence on the concentration of oxygen deficiency and the average oxidation of Mn in the perovskite oxides. Remarkably, compared to the benchmark Pt/C catalyst, $CaMnO_{3-\delta}$ nanoparticles with δ of ~0.25 showed a very close ORR activity in terms of low overpotential and 4e reduction process. The high catalytic performance was associated with enhanced intrinsic electrical conductivity and favored oxygen activation, as confirmed by coupling experimental studies and density functional theory (DFT) calculations.

■ EXPERIMENTAL SECTION

Material Synthesis. Chemical reagents of calcium carbonate, calcium nitrate, manganese nitrate (50% aqueous solution), ammonium carbonate, ammonium bicarbonate, nitric acid, ethylene glycol, citric acid, isopropanol (99.5%), ethanol (99.9%), and Nafion (5% in a mixture of lower aliphatic alcohols and water) were all purchased from Sigma-Aldrich. Carbon-supported Pt nanoparticles (Pt/C, 30 wt % Pt) were supplied by Johnson Matthey Company. The preparation of pristine $CaMnO_3$ microspheres consists of a two-step route:[29,32] Synthesis of calcite $CaMn(CO_3)_2$ precursor through a coprecipitation method and calcination of $CaMn(CO_3)_2$ to form $CaMnO_3$ microspheres. In a typical synthesis, the precursors were first synthesized by dissolving fresh manganese(II) carbonate (1 mmol) and calcium carbonate (1 mmol) in 10.5 mL of 0.5 M dilute nitric acid. Subsequently, 5.25 mL of 0.25 M $(NH_4)_2CO_3$ aqueous solution was dripped, and the resulting solution was vigorously stirred for 30 min and aged for 3 h at room temperature. Precipitates were centrifuged, washed, vacuum-dried, and calcined at 900 °C in air for 5 h to obtain pristine $CaMnO_3$ microspheres. This $CaMnO_3$ was used as a starting material for the synthesis of nonstoichiometric $CaMnO_{3-\delta}$ ($0 < \delta \leq 0.5$) through a heat treatment in a H_2/Ar (5%/95%) forming gas.[33] A set of samples were obtained by heating pristine $CaMnO_3$ in 5% H_2/95% Ar atmosphere at different temperatures (250, 300, and 350 °C) for varied time (2, 5, and 10 h). For example, $CaMnO_{2.90}$ microspheres were obtained by heating $CaMnO_3$ in 5% H_2/95% Ar atmosphere at 250 °C for 5 h. Table S1, Supporting Information lists the details of experimental conditions and synthetic parameters for the other samples. To avoid possible reoxidation, the reducing atmosphere was maintained until the product was naturally cooled down to room temperature.

In comparison, pristine nanoparticulated $CaMnO_3$ was prepared by the Pechini route, which was also subjected to thermal reduction to afford oxygen deficiency. Pristine nanoparticulated $CaMnO_3$ was synthesized as follows. $Ca(NO_3)_2 \cdot 4H_2O$ (4 mmol) and $Mn(NO_3)_2$ (4 mmol) were dissolved in 20 mL of deionized water. After citric acid (8 mmol) and ethylene glycol (5 mL) were added under stirring, the solution was vigorously stirred under 85 °C in water bath for 6 h. A yellow gel-like precipitate was collected and dried at 80 °C overnight. The obtained precursor was further annealed at 900 °C for 5 h under air atmosphere to obtain the pristine $CaMnO_3$ nanoparticles. A set of samples with different compositions were also obtained by adjusting annealing temperatures and dwell time in 5% H_2/95% Ar atmosphere (Table S1).

Material Characterization. The crystal structure analyses were characterized by powder X-ray diffraction (XRD, Rigaku Mini Flex 600 X-ray generator, Cu Kα radiation, λ = 1.5406 Å) at a scanning rate of 4° min^{-1} from 10 to 80°. SEM images were taken on a JEOL JSM-7500F microscope (operating voltage, 5 kV). TEM images were performed on Philips Tecnai F20 operated at 200 kV and JEOL JSM-2010 microscopes equipped with the high resolution electron energy loss spectroscopy (EELS). EELS spectra were obtained with a Gatan Image Filter model 2001. The oxygen-deficient content δ value and the oxidation state of Mn were measured by chemical titration. Typically, the obtained samples (15 mg) were dissolved in the mixed solution of 15 mL of 0.5 M sulfuric acids, 10 mL of 0.1 M phosphoric acids, and 10 mL of 0.05 M $Fe(NH_4)_2(SO_4)_2$ solution. The resulting solution was titrated with calibrated $KMnO_4$ solution.[34] Atomic adsorption spectrometry was tested on a Hitachi 180-80 spectrometry. Elemental analysis was measured by inductively coupled plasma-atomic emission spectroscopy (ICP 9000, Thermo Jarrell Ash Corp). In ICP analyses, 0.5 M sulfuric acids and 0.1 M phosphoric acids were used to dissolve the samples. Thermogravimetric analysis was carried out on a NETZSCH STA 449F3 using a heating rate of 5 °C min^{-1} from 25 to 350 °C in air stream. Mn k-edge (6540 eV) X-ray adsorption spectroscopy (XAS) was performed in BL14W1 beamline of Shanghai Synchrotron Radiation Facility (SSRF). Powder samples were uniformly pasted onto a metal free tape (3M Scotch 810-R). The white beam of the bending magnet was monochromatized by a Si (111) double monochromator. The absorption spectra were collected using a transmission mode near the K-edge of Mn by stepping the Si (111) monochromator. Data management of X-ray absorption near edge spectroscopy (XANES) and extended X-ray adsorption fine spectroscopy (EXAFS) was conducted using a software Ifeffit Athena and Artemis. In Athena, EXAFS r-space data were obtained from Fourier transformed (FT) of energy normalized k_3-weighted XANES data, of which backgrounds and pre-edge were already removed. X-ray photoelectron spectroscopy (XPS) measurements were performed using a Kratos Axis Ultra DLD spectrometer employing a monochromated Al−Kα X-ray source ($h\nu$ = 1486.6 eV), hybrid (magnetic/electrostatic) optics, and a multichannel plate and delayline detector (DLD). The conductivity of the prepared sample was measured by a four-probe meter detector (China, RTS-8) at room temperature. The specific surface area was determined by nitrogen adsorption−desorption measurement at 77 K (Japan, BELSORP-Mini).

Electrochemical Tests. Electrochemical measurements were carried out with a computer-controlled workstation bipotentiostats (AFCBP1, Pine Instrument) assembled with a modulated speed rotator (PHYCHEMI) in a three electrode cell configuration under room temperature. Saturated calomel electrode (SCE) and Pt wire (or graphite rod) were used as the reference and counter electrode, respectively. The working electrode was a glassy carbon electrode coated with a thin layer of catalyst, which was prepared by ultrasonically mixing 10.0 mg of the as-prepared catalyst with 50 μL of Na^+-exchanged Nafion solution and 950 μL of isopropanol solvent for 30 min in order to make a homogeneous suspension. Then, 6.0 μL of the prepared catalytic suspension was loaded onto the surface of a rotation ring-disk electrode (RRDE) of 5.61 mm diameter using a micropipette. Finally, the ink was allowed to dry overnight under ethanol atmosphere at room temperature to form a thin catalyst film. To improve the conductivity, the prepared samples were mixed with 70 wt % of carbon powders (Cabot Vulcan XC-72) while fixing the weight of the total catalyst mixture. Catalyst loading is approximately 0.073 mg cm^{-2} for RRDE. For comparison, electrocatalytic performance of the benchmark Pt/C (30 wt % Pt, Johnson Matthey) was also investigated under the same condition. Voltammetry and RRDE studies were carried out in 0.1 M aqueous KOH electrolyte saturated with high-purity O_2 or Ar. In our tests, at least three parallel electrochemical measurements were performed for each sample to ascertain the reproducibility. The required atmosphere was held above the electrolyte throughout the measurements. In RRDE tests, a constant potential of 1.5 V (versus RHE) was applied at the Pt ring electrode for detecting the oxidation current of the intermediate

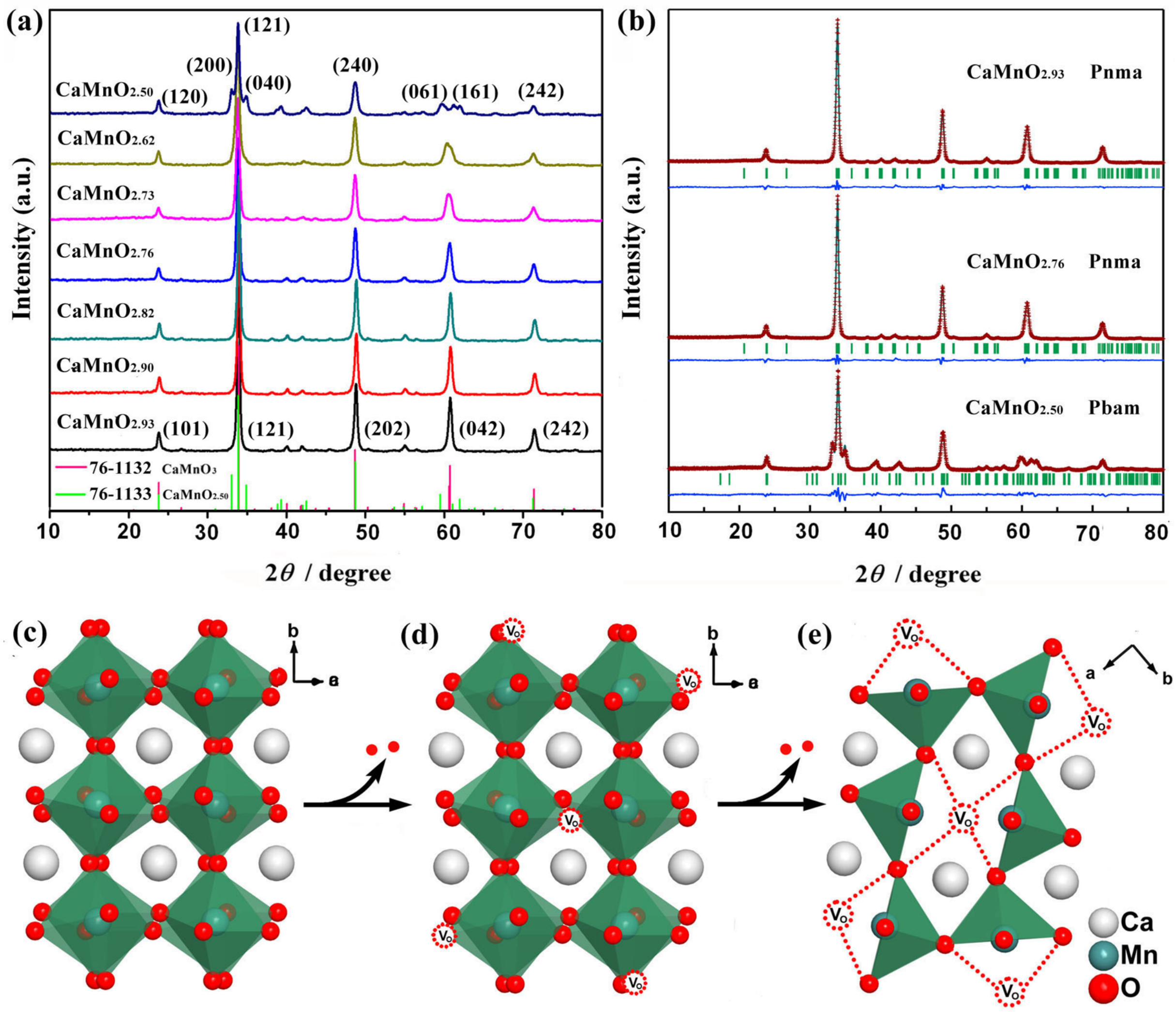

Figure 1. (a) Powder XRD patterns of the as-prepared $CaMnO_{3-\delta}$ ($0 < \delta \leq 0.5$) samples. (b) Rietveld refined XRD patterns of $CaMnO_{2.93}$, $CaMnO_{2.76}$, and $CaMnO_{2.5}$, with experimental data (red dots), calculated profile (cyan lines), allowed positions of Bragg reflection (green vertical bars) and difference curves (blue lines). (c−e) Schematic representation of the crystal frameworks of pristine and oxygen-deficient perovskite oxides showing a transition from stoichiometric $CaMnO_3$ (c) to nonstoichiometric $CaMnO_{2.76}$ (d) and $CaMnO_{2.5}$ (e).

peroxide species generated at the working disk electrode. Unless otherwise stated, all potentials were reported with reference to the reversible hydrogen electrode (RHE) potential. In 0.1 M KOH solution, the potential of SCE was calibrated as +0.990 V with respect to RHE. Voltammograms were collected from 1.1 to 0.4 V under a scanning rate of 5 mV s^{-1} at 400, 625, 900, 1225, 1600, and 2025 rpm (revolution per minute). Electrochemical impedance spectra were obtained over a frequency range of 100 kHz to 100 mHz at a DC bias potential of 0.7 V at room temperature. Chronoamperograms were measured at 0.7 V with an electrode rotating rate of 400 rpm.

Computational Details. All calculations were performed by the Vienna ab initio simulation package (VASP)[35] using periodic density functional theory (DFT). Projector augmented wave (PAW) method[36] was employed to describe the valence-electron interactions. To gain exact description of electronic structures, density of states (DOS) calculation was performed with the Heyd−Scuseria−Ernzerhof (HSE06) hybrid functional[37] containing 25% of the exact Hartree−Fock (HF) exchange and 75% of the Perdew−Burke−Ernzerhof (PBE) exchange functional, which is widely used in computing manganese oxides.[38] Generalized gradient approximation (GGA) of Perdew−Wang 1991 (PW91) was supplemented for structure optimization by the rotationally invariant "+U" description of Dudarev et al.[39] Energy cutoff was set to 400 eV and electron smearing was employed using Gaussian smearing technique with a width of 0.2 eV. The Hubbard U value of Mn atoms was chosen as 4.5 eV, according to previous literature reports.[38,40,41] Only Gamma point was used in the calculation, which is appropriate for finite models. Spin polarization calculation was carried out for all possible structures with the bottom two layers of the surface fixed. The lattice parameters of the $CaMnO_{3-\delta}$ compounds were referenced to experimental values. To investigate oxygen adsorption, surface models with 15.0 Å of a vacuum layer are used and the most stable surfaces are referenced to XRD information, which is (121) for both $CaMnO_3$ and $CaMnO_{2.75}$. Electronic energies were computed with the self-converged field (SCF) tolerance of 10^{-5} eV, and total forces were converged to less than 0.03 eV/Å.

■ RESULTS AND DISCUSSION

Composition, Structure and Morphology. Figure 1a displays the powder XRD patterns of the synthesized $CaMnO_{3-\delta}$ ($0 < \delta \leq 0.5$) samples. The oxides with $\delta < 0.5$ present similar profiles, which correspond to a typical pervoskite phase (standard $CaMnO_3$, JCPDS No. 76-1132). In comparison, the peaks of $CaMnO_{2.5}$ are indexable to a different structure (JCPDS No. 76-1133), with characteristic splitting peaks around 2θ deg of 34° and 60°. Figure 1b shows the Rietveld refinement of XRD data for representative

$CaMnO_{2.93}$, $CaMnO_{2.76}$, and $CaMnO_{2.5}$, which can be structurally defined in the orthorhombic *Pnma* and *Pbam* space groups with good fitting. Among the $CaMnO_{3-\delta}$ ($\delta < 0.5$) series, their refined lattice parameters show a trend of expansion with increasing oxygen nonstoichiometry, as could be anticipated due to the formation of more Mn^{3+} with larger radius.

Figure 1c−e schematically depicts the crystal structures of three typical Ca−Mn−O oxides. In stoichiometric $CaMnO_3$, each Mn^{4+} ion is coordinated by six oxygen anions, forming corner-sharing MnO_6 octahedra (Figure 1c). For oxygen-deficient $CaMnO_{3-\delta}$, the loss of oxygen is accompanied by the reduction of Mn^{4+} to Mn^{3+} cations. The framework of the perovskite structure is essentially maintained for oxides with $\delta < 0.5$ (Figure 1d), as previously suggested.[33] In comparison, $CaMnO_{2.5}$ adopts a different structure, in which all MnO_6 octahedra are transformed into MnO_5 square pyramids (Figure 1e). Regardless of the elimination of some oxygen atoms, the cationic structural framework and remaining anionic sublattice are basically preserved. The perovskite-related Ca−Mn−O phase transformation can be viewed as a topotactic reduction process.[32−34,42] Chemical composition of $CaMnO_{3-\delta}$ was determined by coupling chemical titration and atomic adsorption spectrometry. The stoichiometry deviation in the oxide was also revealed by TGA (Figure S1, Supporting Information) performed in air atmosphere, where the weight gain due to reoxidation coincided well with that expected from the nominal composition. On the basis of the invariable valence of Ca, the nonstoichiometry could be further confirmed by the oxidation state of Mn, which is discussed later in the section of energy spectroscopies.

Figure 2 shows the morphologies and microstructures of the as-synthesized $CaMnO_{3-\delta}$ samples. The oxide resulted from thermal decomposition of coprecipitated $CaMn(CO_3)_2$ presents the shape of porous microspheres, which consisted of agglomerated nanoparticles (Figure 2a). The sample prepared through the Pechini route is composed of nanoparticles with an average size of 50 nm (Figure 2b). Morphologies of the oxygen-defective perovskites resemble the corresponding pristine oxides without posttreatment of thermal reduction (Figure S2, Supporting Information). TEM imaging was performed to gain microstructural information. Both samples reveal high crystallinity with clear lattice fringes (Figure 2c,d). The interlayer distances well match the related neighboring separations of (020) and (002) planes, being consistent with the XRD results. The fast Fourier transform (FFT) patterns conform to the orthorhombic perovskite structure. The oxygen vacancies in an oxide are difficult to be detected by typical TEM imaging.[43] However, planar defects can be seen in the inverse FFT images of HRTEM[44] (Figure S3, Supporting Information), which indicate the presence of phase boundaries in nonstoichiometric oxides. As expected, the density of defects increases with higher content of oxygen vacancies.

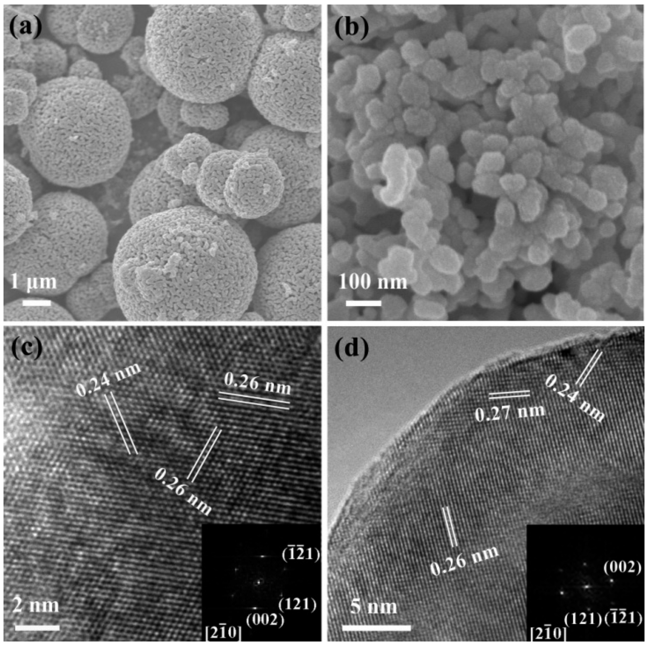

Figure 2. (a, b) SEM and (c, d) high-resolution TEM images with the inset of FFT patterns of $CaMnO_{3-\delta}$ prepared by thermal reduction of pristine $CaMnO_3$ that resulted from carbonate decomposition (a, c) and the Pechini route (b, d).

Energy Spectroscopies. We performed different spectroscopic studies to analyze the oxidation state and chemical environment of Mn in $CaMnO_{3-\delta}$ oxides. Figure 3, panels a and b show respectively the Mn 2p and Mn 3s XPS spectra of three representative samples of $CaMnO_{2.93}$, $CaMnO_{2.76}$, and $CaMnO_{2.5}$. The main results are summarized in Table S2, Supporting Information. Mn 2p spectra of all three samples can be fitted with two deconvoluted peaks, suggesting the existence of multiple Mn valence (Mn^{III} and Mn^{IV}). The sum peak position of Mn $2p_{3/2}$ shifts slightly to lower binding energy side as the oxygen defect increases, indicating a lower Mn valence.[45] The energy splitting (ΔE) of Mn 3s doublet peaks is 4.84, 5.01, and 5.24 eV for $\delta = 0.07$, 0.24, and 0.5, respectively. On the basis of the reported linear relationship between ΔE and oxidation state of Mn,[45] the corresponding Mn valence is 3.9, 3.5 and 3.1, in line with titration analysis.

Figure 3c shows the EELS profiles of $CaMnO_{2.93}$, $CaMnO_{2.76}$, and $CaMnO_{2.5}$ microspheres. The energy shift of the L_3 edge and the energy difference between the L_3 and L_2 edge ($\Delta E_{L2,3}$) in EELS can be used to estimate the Mn valence.[46,47] The energy of the L_3 edge peak maximum shifts to lower energy loss as the oxygen deficiency increases, indicating a decrease of Mn oxidation state. In addition, the $\Delta E_{L2,3}$ values for $CaMnO_{2.93}$, $CaMnO_{2.76}$, and $CaMnO_{2.5}$ are 10.35, 10.52, and 10.75 eV, respectively. The larger energy difference is indicative of a lower average valence of Mn in manganese oxides.[46] Thus, the EELS data follow the trend with the observation of XPS characterization.

The XAS technique is powerful to probe the oxidation state, bond geometry, and metal coordination of electrocatalysts.[48] Inset of Figure 3d illustrates the X-ray absorption near edge structure (XANES) spectra of $CaMnO_{2.93}$, $CaMnO_{2.76}$, and $CaMnO_{2.5}$ microspheres. When the oxygen nonstoichiometry increases in the perovskite, the K-edge position shifts to a lower energy, showing a reduction in the Mn oxidation state. The observed Mn valence is between 3 and 4 for $CaMnO_{2.93}$ and $CaMnO_{2.76}$, while it closely matches 3 for $CaMnO_{2.5}$. This can be seen by comparing their spectra to that of β-$Mn^{IV}O_2$ and Mn_3O_4 reference standards (Figure S4, Supporting Information). The samples of $CaMnO_{2.93}$ and $CaMnO_{2.76}$ display similar XANES profiles, which however obviously differ from that of $CaMnO_{2.5}$. This difference should be associated with their structure variation (i.e., both $CaMnO_{2.93}$ and $CaMnO_{2.76}$ adopts the *Pnma* phase while $CaMnO_{2.5}$ crystallizes into the

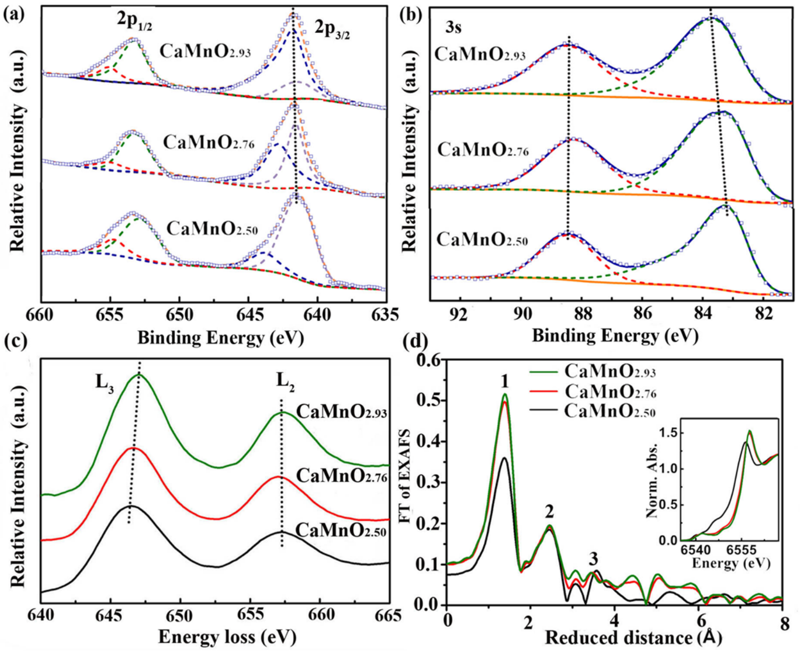

Figure 3. Energy spectroscopies of $CaMnO_{3-\delta}$ (δ = 2.93, 2.76, and 2.50) microspheres: (a) Mn 2p and (b) Mn 3s XPS, (c) Mn L_2 and L_3 EELS, and (d) Mn K-edge XANES (inset) and k_3-weighted Fourier-transformed EXAFS (peaks 1, 2, and 3 relate to Mn−O, Mn−Ca, and Mn−Mn distance, respectively).

Pbnm structure, as shown in Figure 1). Analysis of the extended X-ray absorption fine structure (EXAFS) spectra (Figure 3d) also demonstrates the structural similarity between $CaMnO_{2.93}$ and $CaMnO_{2.76}$ but noticeable discrimination with respect to $CaMnO_{2.5}$. The Fourier transformation of EXAFS data further suggests that Mn ions are coordinated by fewer oxygen ions in $CaMnO_{2.5}$, which contains MnO_5 pyramids and is expected to have a lower coordination number as compared to $CaMnO_3$. As the content of oxygen vacancies increases, slightly elongated Mn−O and Mn−Mn distance is observed as well. Therefore, combining spectroscopies of XPS, EELS, and XAS confirms the valent variation and structural modification of Ca−Mn−O perovskites after controllable introduction of oxygen deficiency.

Electrocatalytic Properties. The cyclic voltammetry (CV) of nonstoichiometric $CaMnO_{3-\delta}$ in O_2 and Ar-saturated 0.1 M aqueous KOH solution was first investigated (Figure S5, Supporting Information). In Ar-saturated 0.1 M KOH solution, the $CaMnO_{2.97}$ exhibits one broaden cathodic peak at ca. 0.84 V, which is ascribed to the Mn^{4+} ions located on the $CaMnO_{2.97}$ surface into Mn^{3+} intermediates (e.g., γ-MnOOH in alkaline media).[11] In the reversed positive cycle, the anodic peak at 0.90 V was observed. The oxidation peak was attributed to the oxidation of the generated Mn^{3+} intermediates into Mn^{4+} ions. In 0.1 M KOH solution saturated with O_2, a well-defined cathodic peak emerges at 0.76 V and exhibits larger peak current. This cathodic peak is thereby logically attributed to the ORR process. The surface redox reaction of Mn-containing species may accompany and mediate the oxygen electrocatalysis process.[11,49]

Figure 4 shows the typical linear sweeping voltammograms (LSVs) in 0.1 M KOH solution saturated with O_2. The curves below 1.1 V correspond to the ORR process, while the OER proceeds above 1.4 V. For both ORR and OER, the perovskite samples with oxygen deficiency outperform the pristine oxides. In the ORR region, the difference in catalytic activities can be clearly seen from the voltametry variation near the half-wave potential region (inset of Figure 4). To reach a specific geometric current density of 1.5 mA cm^{-2}, the potentials are 728, 773, 768, 779, 814, and 831 mV for $CaMnO_{2.93}$ microspheres, $CaMnO_{2.76}$ microspheres, $CaMnO_{2.50}$ microspheres, $CaMnO_{2.90}$ nanoparticles, $CaMnO_{2.77}$ nanoparticles, and Pt/C, respectively. A more positive potential indicates higher activity. Remarkably, the nonstoichiometric $CaMnO_{2.77}$ nanoparticles exhibit ORR performance comparable to the benchmark Pt/C. The measured activity of the benchmark Pt/C catalyst is consistent with reported data (Figure S6, Supporting Information).[10,50] For the OER, introducing oxygen vacancies affords an even more prominent improvement in performance with significantly reduced overpotentials and

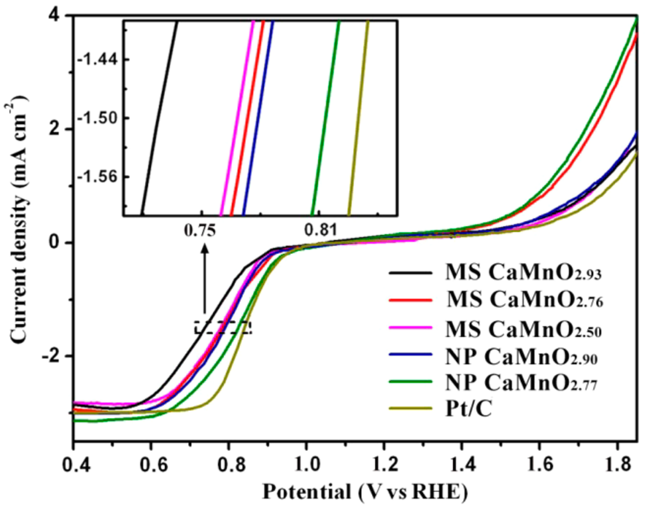

Figure 4. Bifunctional OER/ORR electrocatalytic activities of $CaMnO_{3-\delta}$ microspheres (MS), nanoparticles (NP), and the comparative Pt/C in O_2-saturated alkaline solution. The inset enlarges the ORR curves in the half-wave potential region.

Table 1. Mass Activities (MA) and Specific Activities (SA) Measured at 0.7 V (for the ORR) and 1.7 V (for the OER) vs. RHE, and Electrical Conductivity of Different $CaMnO_{3-\delta}$ Samples

	ORR (0.7 V vs RHE)		OER (1.7 V vs RHE)		
sample	MA (A g^{-1})	SA (A m^{-2})	MA (A g^{-1})	SA (A m^{-2})	electrical conductivity (S m^{-1})
MS $CaMnO_{2.93}$	25.91 ± 0.15	0.78 ± 0.01	10.03 ± 0.12	0.31 ± 0.01	1.56×10^{-3}
MS $CaMnO_{2.76}$	31.22 ± 0.20	0.86 ± 0.02	21.68 ± 0.13	0.60 ± 0.02	4.86×10^{-2}
MS $CaMnO_{2.50}$	32.06 ± 0.20	0.84 ± 0.02	9.74 ± 0.08	0.27 ± 0.01	1.80×10^{-3}
NP $CaMnO_{2.90}$	33.31 ± 0.23	0.87 ± 0.03	11.25 ± 0.12	0.29 ± 0.01	2.62×10^{-3}
NP $CaMnO_{2.77}$	36.79 ± 0.20	0.92 ± 0.03	24.7 ± 0.14	0.65 ± 0.02	4.67×10^{-2}
Pt/C	39.02 ± 0.25	0.61 ± 0.01	7.82 ± 0.06	0.12 ± 0.01	

increased anodic currents. The OER overpotential of nanoparticulated $CaMnO_{2.77}$ catalyst (~1.50 V at 10 A/g_{ox} and ~1.60 V at 50 μA/cm^2_{ox} normalized to electrochemical activity surface area, Figure S6) is comparable to that of reported $Ba_{0.5}Sr_{0.5}Co_{0.8}Fe_{0.2}O_{3-\delta}$ (BSCF),[23] but its OER activity at 1.50 V is still 10-fold lower than the fastest water oxidation catalyst ($Ni_{1-x}Fe_xOOH$ materials) known in basic media.[51] Figure S7, Supporting Information shows the ORR voltammetry and the OER linear sweeping curves of $CaMnO_{2.77}$ nanoparticles before and after 10 cyclic voltammograms (CVs) of OER tests. Negligible change of the OER and ORR kinetics is observed after repeated OER cycles on $CaMnO_{2.77}$ nanoparticles, which indirectly suggests favorable chemical durability of the nonstoichiometric oxide catalyst. Furthermore, Mn valence also remains unchanged from the analysis of the Mn 2p and Mn 3s XPS spectra of $CaMnO_{2.77}$ nanoparticles (Figure S8, Supporting Information). The samples of nanoparticles have superior activities to microspheres, which is possibly attributed to the higher specific surface areas (Figure S9, Supporting Information, 22.0 vs 9.20 m^2 g^{-1}). The ORR and OER mass activity and specific activity (based on the electrochemical activity surface area, Figure S6) of the prepared catalysts are also summarized in Table 1. Improved mass activity and specific activity can be observed for nonstoichiometric oxide catalyst in comparison with the benchmark Pt/C.

To further demonstrate the influence of oxygen vacancy into the ORR activity, we performed a systematical investigation on the electrolytic activities of nonstoichiometric $CaMnO_{3-\delta}$ (δ = 0.07, 0.10, 0.18, 0.24, 0.27, 0.38, and 0.5) microspheres with similar morphologies, sizes, and surface areas. Figure S10 shows the linear sweeping voltammograms (LSVs) and the kinetic current density of ORR activity for all nonstoichiometric $CaMnO_{3-\delta}$. The sample of $CaMnO_{2.76}$ with a modest concentration of oxygen vacancy (δ = 0.24), which is featured with an average Mn valence of ~3.5, exhibited the highest ORR activity. This value is different from that predicted by the molecular-orbital approach. It was reported that transition-metal-oxide perovskites having an e_g-filling value of ~1 showed the highest activity, implying the preferable Mn valence of ~3.0 for manganese perovskites.[52] Thus, other factors beyond Mn valence should be taken into consideration to correlate with the catalytic performance of $CaMnO_{3-\delta}$. The oxygen activation and electrical conductivity also influence the activity, as seen from the last section of discussion.

We performed RRDE measurements to further study the ORR electrocatalytic properties and the reduction pathway. As the nanoparticles show superior specific geometric activities to that of the microspheres, we selected nanoparticles for further investigation. Figure 5a displays the voltammograms collected on the disk and ring electrodes by subtracting the background currents recorded in Ar-saturated electrolyte. While the disk valtametry directly reflects the catalytic ORR, the ring currents are indicative of the yield of peroxide species (i.e., HO_2^-). Figure 5b shows the values of percentage of peroxides with respect to the total oxygen reduction products ($P_{HO_2^-}$) and the electron transfer number (n) involved in the ORR. For all samples, the determined average electron transfer numbers are above 3.90 within the measured potential range, suggesting that the catalytic ORR proceeds mainly through an apparent four electron (4e) pathway. The percentage of generated peroxide species is less than 4%. Notably, the synthesized $CaMnO_{2.77}$ nanoparticles enable even higher electron transfer number and lower peroxide yield than that of the benchmark Pt/C. Furthermore, the ORR kinetics can be evaluated from the Koutechky−Levich (K−L) plots (Figure 6a) using the currents

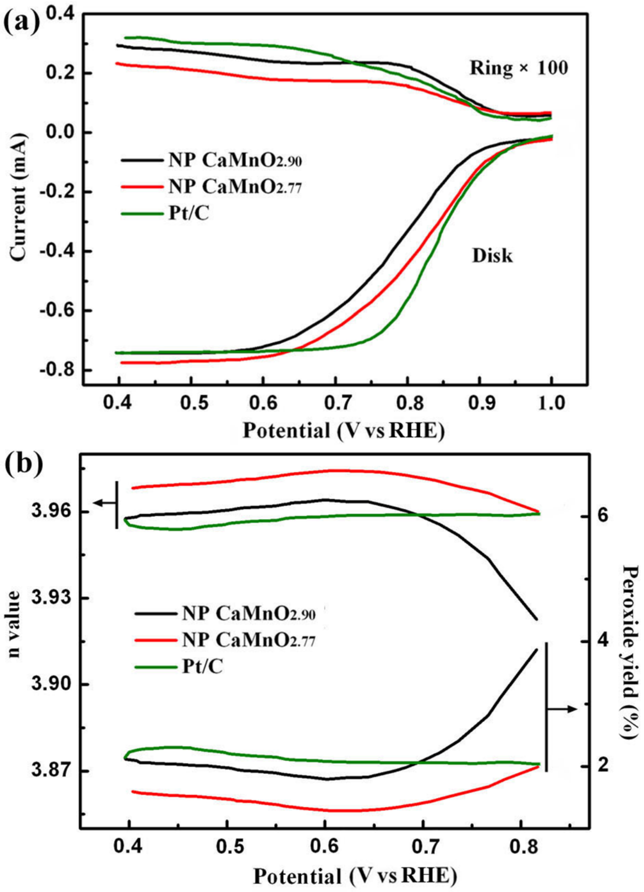

Figure 5. RRDE results for nanoparticles (NP) of $CaMnO_{2.90}$ and $CaMnO_{2.77}$, and Pt/C catalyst at a rotational rate of 400 rpm: (a) Voltammetry recorded on the disk and ring electrodes; (b) calculated electron transfer number and percentage of generated peroxide relative to the total product.

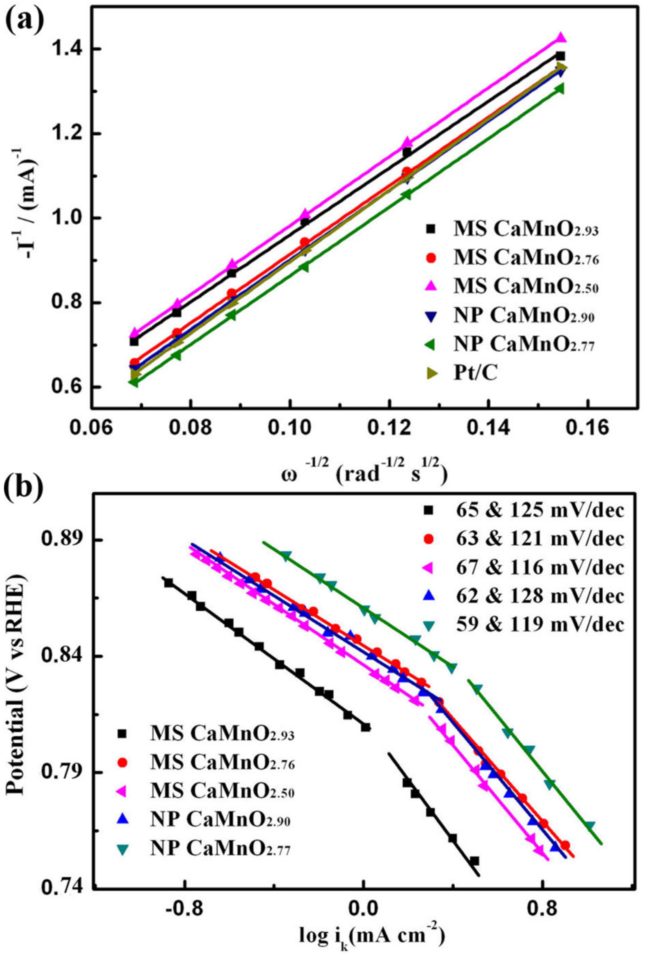

Figure 6. (a) K–L plots of $CaMnO_{3-\delta}$ microspheres (MS), nanoparticles (NP), and the comparative Pt/C at applied potential of 0.74 V. (b) Tafel plots of $CaMnO_{3-\delta}$ microspheres (MS) and nanoparticles (NP) derived by the mass-transport correction of voltammetry data.

that depend on rotation speed of the electrode (Figure S11, Supporting Information). The plots of all samples show good linearity. Using the slopes of these lines, the electron transfer number n is calculated to be close to 4 for all perovskite samples and the benchmark Pt/C catalyst, again suggesting an overall 4e ORR pathway. For the nanoparticulated $CaMnO_{2.77}$, the intercept of the plot reveals a larger kinetic current, further indicating its high catalytic activity.

Additionally, according to the mass-transport correction, the kinetic currents for all $CaMnO_{3-\delta}$ catalysts were used to construct the Tafel plots (Figure 6b). Two Tafel slopes can be observed at high and low overpotentials, respectively. The corresponding slopes are close to the theoretical values of $-2.303RT/F$ and $-2.303(2RT/F)$, where R is the universal gas constant, F is the Faraday constant, and T is absolute temperature. The Tafel behavior indicates similar reaction pathway and rate-determining step for the catalysts, which is consistent with reported results for other Mn-based ORR catalysts.[11,29] Besides high activity, the nonstoichiometric perovskite oxides also exhibited respectable catalytic stability in alkaline electrolyte. At a constant voltage of 0.7 V, the ORR current density generated by $CaMnO_{2.77}$ nanoparticles sustained more than 88% over 30 h of continuous operation, while the Pt/C counterpart exhibited a quick current decay of about 20% (Figure S12, Supporting Information). From the elemental analysis of the electrolytes after electrochemical stability measurements, Ca and Mn were not detectable, indicating negligible leaching of cations during tests. Furthermore, the morphology of the catalyst was preserved after the stability test, as verified by SEM images of $CaMnO_{2.77}$ before and after stability test (Figure S13, Supporting Information).

Lastly, we carried out the electrochemical impedance spectroscopy measurements for pristine $CaMnO_{2.93}$ and thermal-reduced $CaMnO_{2.76}$ catalysts in the ORR (Figure S14, Supporting Information). In the Nyquist plots collected at 0.7 V, $CaMnO_{2.76}$ showed a smaller compressed semicircle than that of the pristine $CaMnO_{2.93}$, which suggests a lower charge transfer resistance of $CaMnO_{2.76}$ during the electrocatalytic process. The lowered charge transfer resistance, which improves the ORR catalysis, is likely due to the higher electrical conductivity that favors shuttling charges from catalyst to oxygen.[53] In view of the results, we measured the electrical conductivity of $CaMnO_{3-\delta}$ microspheres (Table S3, Supporting Information). The conductivity of $CaMnO_{2.76}$ is the highest among the tested oxides having either higher or lower concentration of oxygen vacancies, consistent with literature results.[54] The enhanced electrical conductivity can be also understood from the multiple oxidation states of Mn. In $CaMnO_{2.75}$, Mn ions (with nominal valence of 3.5) can be viewed to coexist in the forms of Mn^{3+} and Mn^{4+} in equivalent molar ratio, which could impart a higher concentration of charge carriers[55] and contributes to the improvement in electronic transport. Thus, the most efficient $CaMnO_{3-\delta}$ catalyst features the highest electrical conductivity. Furthermore, the presence of oxygen deficiency in the perovskite should be another beneficial factor for enhanced catalytic activity. Recently, we have demonstrated that a modest concentration of oxygen vacancies in rutile-type MnO_2 affords modified surface-oxygen interaction and reduced activation barrier for the ORR.[56] Likewise, the Ca–Mn–O perovskite oxide bearing with a median oxygen nonstoichiometry can probably facilitate O_2-oxide interaction and improve the ORR kinetics.

Accordingly, we then performed DFT studies to investigate the electronic structures of $CaMnO_{3-\delta}$ and the structure of oxygen adsorbed on $CaMnO_{3-\delta}$. DFT modeling is a useful tool to understand the electrochemical behaviors of manganese oxides.[55,57] Figure 7 shows the calculated density of states (DOS) of stoichiometric $CaMnO_3$ (without oxygen vacancy), $CaMnO_{2.75}$ (one oxygen vacancy per unit cell) and $CaMnO_{2.5}$ (two oxygen vacancies per unit cell). A band gap (E_g) of approximately 1.56 eV is observed for $CaMnO_3$, which indicates a semiconducting behavior and is in good agreement with reported experimental result of E_g = 1.55 eV.[58] As to $CaMnO_{2.75}$, the DOS profile changes significantly. Near the Fermi level, states exist for spin-up while there is a gap for the spin-down states. Such a large spin polarization implies a half metallicity, which can benefit the electrical conduction in metal oxides.[59] In the case of $CaMnO_{2.5}$, despite spin polarization, no obvious states are positioned at the Fermi level, demonstrating insignificant half-metal properties relative to $CaMnO_{2.75}$. The DFT calculated results are also consistent with the experimental results and literature data.[54]

Figure 8 shows the DFT calculated structures of O_2 adsorbed on the $CaMnO_3$ and $CaMnO_{2.75}$ surfaces, respectively. Oxygen molecule is bound to the surface Mn atoms through a Griffith

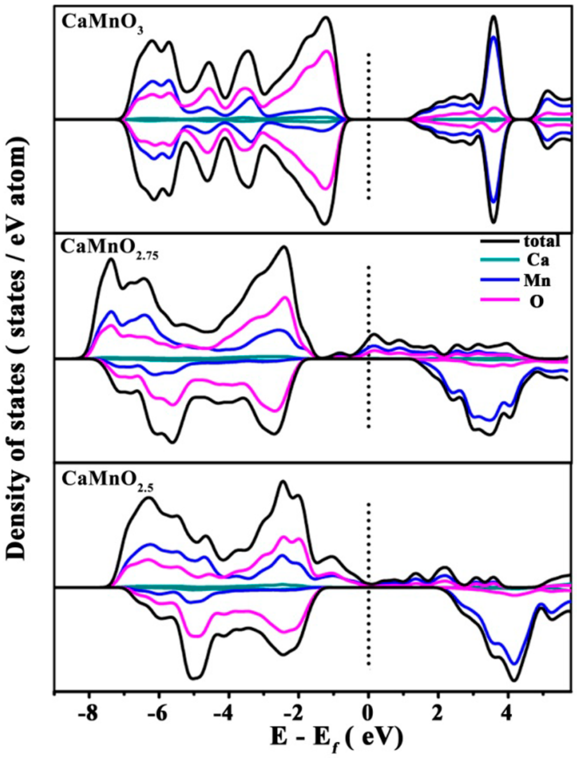

Figure 7. DFT calculation of the density of states (DOS) of pristine $CaMnO_3$, $CaMnO_{2.75}$, and $CaMnO_{2.5}$.

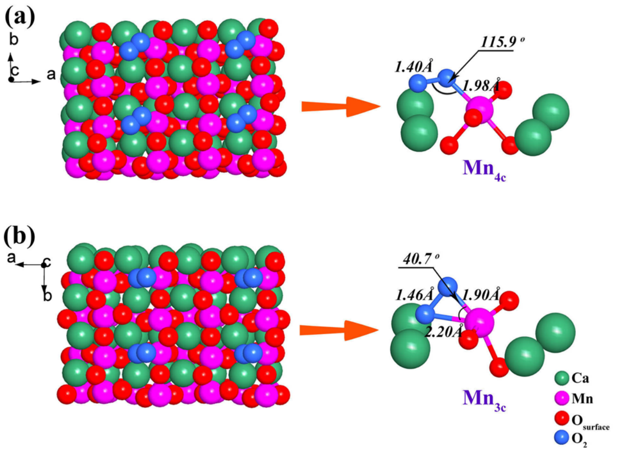

Figure 8. Top view of the configuration of molecular oxygen adsorbed on (a) $CaMnO_3$ (121) surface and (b) $CaMnO_{2.75}$ (121) surface. The right parts are the bond length information after oxygen adsorbed on the surfaces. The green, pink, and red spheres are used to represent Ca, Mn, and lattice O atoms respectively, and the adsorbed oxygen molecule is shown in blue.

(side-on) manner on $CaMnO_{2.75}$ surface, favoring the rupture of the O−O bond (with length of 1.46 Å).[19] In comparison, Pauling (end-on) form occurs when oxygen adsorbed on the $CaMnO_3$ surface. The O−O bond length is 1.40 Å, shorter than that on $CaMnO_{2.75}$ surface. The preliminary DFT modeling reveals that the O−O bond elongation of adsorbed oxygen molecules is more prominent on the surface of oxygen-vacant $CaMnO_{2.75}$ than the stoichiometric $CaMnO_3$. This result indicates the O_2 activation of $CaMnO_{2.75}$ is stronger than $CaMnO_3$. Thus, the activity of oxygen-vacant $CaMnO_{2.75}$ is more beneficial than the stoichiometric $CaMnO_3$. This is consistent with the electrochemical results.

■ CONCLUSION

We report on the synthesis and characterization of a series of nonstoichiometric perovskite-type calcium−manganese oxides ($CaMnO_{3-\delta}$, $0 < \delta \leq 0.5$) with the morphologies of microspheres and nanoparticles. The nonstoichiometric $CaMnO_{3-\delta}$ offered the opportunity to investigate the role of variable Mn valence state and oxygen deficiency in electrocatalysis of oxygen reduction reactions and oxygen evolution reactions (ORR/OER). In particular, the oxygen-defective $CaMnO_{3-\delta}$ with δ close to 0.25 and average Mn valence near ∼3.5 manifests the most ORR catalytic activity (36.7 A g^{-1} at 0.70 V vs RHE). Computational studies and electrical conductivity test further confirm that the superior catalytic activity of $CaMnO_{2.75}$ over the pristine $CaMnO_3$ is mainly attributed to enhanced activation of O_2 and improved electrical conductivity. All these beneficial factors contribute to reduce kinetic barrier of the ORR on nonstoichiometric $CaMnO_{3-\delta}$. In addition, the moderate oxygen-vacant $CaMnO_{3-\delta}$ ($\delta \approx 0.25$) also favors the OER due to the improved electrical conductivity. In view of the enhanced electrocatalytic performance, the oxygen-vacant $CaMnO_{3-\delta}$ is an attractive nonprecious ORR catalytic material alternative to traditional Pt/C catalysts and should find promising applications in diverse oxygen-based energy storage and conversion technologies such as rechargeable metal-air batteries. Furthermore, we expect this catalyst design with appropriate nonstoichiometry to be applicable to other 3d transition-metal oxides for the oxygen electrocatalysis.

■ ASSOCIATED CONTENT

S Supporting Information

Thermogravimetric analysis, SEM and TEM images, Mn K-edge XANES of reference standards, cyclic voltammograms, ORR polarization curves, Mn XPS, N_2 adsorption/desorption isotherms, chronoamperometric curves, and electrochemical impedance spectra data. This material is available free of charge via the Internet at http://pubs.acs.org.

■ AUTHOR INFORMATION

Corresponding Author

*Fax: +86-22-23509571. Tel: +86-22-23506808. E-mail: chenabc@nankai.edu.cn.

Notes

The authors declare no competing financial interest.

■ ACKNOWLEDGMENTS

This study was supported by the National Programs of 973 (2011CB935900), 863 (2012AA051901 and 2012AA051503), NSFC (21231005 and 21322101), and MOE (113016A, B12015 and IRT13R30).

■ REFERENCES

(1) Kinoshita, K. *Electrochemical Oxygen Technology*; Wiley: New York, 1992.

(2) Linden, D.; Reddy, T. B. *Handbook of Batteries*, 3rd ed.; McGraw-Hill: New York, 2002.

(3) Debe, M. K. *Nature* **2012**, *486*, 43.

(4) Chen, Z. W.; Higgins, D.; Yu, A.; Zhang, L.; Zhang, J. J. *Energy Environ. Sci.* **2011**, *4*, 3167.

(5) Cheng, F. Y.; Chen, J. *Chem. Soc. Rev.* **2012**, *41*, 2172.

(6) Zhang, T. R.; Tao, Z. L.; Chen, J. *Mater. Horiz.* **2014**, *1*, 196.

(7) Liang, Y.; Wang, H.; Zhou, J.; Li, Y.; Wang, J.; Regier, T.; Dai, H. J. *J. Am. Chem. Soc.* **2012**, *134*, 3517.

(8) Wu, J.; Xue, Y.; Yan, X.; Yan, W. S.; Cheng, Q. M.; Xie, Y. *Nano Res.* **2012**, *5*, 521.

(9) Du, J.; Cheng, F. Y.; Wang, S. W.; Zhang, T. R.; Chen, J. *Sci. Rep.* **2014**, *4*, 4386.

(10) El-Deab, M. S.; Ohsaka, T. *Angew. Chem., Int. Ed.* **2006**, *45*, 5963.

(11) Roche, I.; Chaînet, E.; Chatenet, M.; Vondrák, J. *J. Phys. Chem. C* **2007**, *111*, 1434.

(12) Cheng, F. Y.; Su, Y.; Liang, J.; Tao, Z. L.; Chen, J. *Chem. Mater.* **2010**, *22*, 898.

(13) Cheng, F. Y.; Zhao, J. Z.; Song, W.; Li, C. S.; Ma, H.; Chen, J.; Shen, P. W. *Inorg. Chem.* **2006**, *45*, 2038.

(14) Tompsett, D. A.; Parker, S. C.; Islam, M. S. *J. Am. Chem. Soc.* **2014**, *136*, 1418.

(15) Lima, F. H. B.; Calegaro, M. L.; Ticianelli, E. A. *Electrochim. Acta* **2007**, *52*, 3732.

(16) Benbow, E. M.; Kelly, S. P.; Zhao, L.; Reutenauer, J. W.; Suib, S. L. *J. Phys. Chem. C* **2011**, *115*, 22009.

(17) Cheng, F. Y.; Chen, J. *Acta Chim. Sinica* **2013**, *71*, 473.

(18) Robinson, D. M.; Go, Y. B.; Mui, M.; Gardner, G.; Zhang, J.; Mastrogiovanni, D.; Garfunkel, E.; Li, J.; Greenblatt, M.; Dismukes, G. C. *J. Am. Chem. Soc.* **2013**, *135*, 3494.

(19) Post, J. E. *Proc. Natl. Acad. Sci. U.S.A.* **1999**, *96*, 3447.

(20) Roche, I.; Chaînet, E.; Chatenet, M.; Vondrák, J. *J. Appl. Electrochem.* **2008**, *38*, 1195.

(21) Bockris, J. O.; Otagawa, T. *J. Electrochem. Soc.* **1984**, *131*, 290.

(22) Oh, S. H.; Black, R.; Pomerantseva, E.; Lee, J. H.; Nazar, L. F. *Nat. Chem.* **2012**, *4*, 1004.

(23) Suntivich, J.; May, K. J.; Gasteiger, H. A.; Goodenough, J. B.; Shao-Horn, Y. *Science* **2011**, *334*, 1383.

(24) Hardin, W. G.; Slanac, D. A.; Wang, X. Q.; Dai, S.; Johnston, K. P.; Stevenson, K. J. *J. Phys. Chem. Lett.* **2013**, *4*, 1254.

(25) Cheng, F. Y.; Shen, J.; Peng, B.; Pan, Y. D.; Tao, Z. L.; Chen, J. *Nat. Chem.* **2011**, *3*, 79.

(26) Ferreira, K. N.; Iverson, T. M.; Maghlaoui, K.; Barber, J.; Iwata, S. *Science* **2004**, *303*, 1831.

(27) McEvoy, J. P.; Brudvig, G. W. *Chem. Rev.* **2006**, *106*, 4455.

(28) Najafpour, M. M.; Ehrenberg, T.; Wiechen, M.; Kurz, P. *Angew. Chem., Int. Ed.* **2010**, *49*, 2233.

(29) Han, X. P.; Zhang, T. R.; Du, J.; Cheng, F. Y.; Chen, J. *Chem. Sci.* **2013**, *4*, 368.

(30) Pérez-Flores, J. C.; Pérez-Coll, D.; García-Martín, S.; Ritter, C.; Mather, G. C.; Canales-Vázquez, J.; Gálvez-Sánchez, M.; García-Alvarado, F.; Amador, U. *Chem. Mater.* **2013**, *25*, 2484.

(31) Ullmann, H.; Trofimenko, N.; Tietz, F.; Stöver, D.; Ahmad-Khanlou, A. *Solid State Ionics* **2000**, *138*, 79.

(32) Reller, A.; Thomas, J. M.; Jefferson, D. A.; Uppal, M. K. *Proc. R. Soc. London A* **1984**, *394*, 223.

(33) Glaunsinger, W. S.; Horoeitz, H. S.; Longo, J. M.; Chang, A. *J. Solid State Chem.* **1980**, *35*, 187.

(34) Zeng, Z.; Greenblatt, M.; Croft, M. *Phys. Rev. B* **1999**, *59*, 8784.

(35) Kresse, G.; Furthmüller, J. *Phys. Rev. B* **1996**, *54*, 11169.

(36) Blöchl, P. E. *Phys. Rev. B* **1994**, *50*, 17953.

(37) Heyd, J.; Scuseria, G. E.; Ernzerhof, M. *J. Chem. Phys.* **2003**, *118*, 8207.

(38) Franchini, C.; Podloucky, R.; Paier, J.; Marsman, M.; Kresse, G. *Phys. Rev. B* **2007**, *75*, 195128.

(39) Dudarev, S. L.; Botton, G. A.; Savrasov, S. Y. *Phys. Rev. B* **1998**, *57*, 1505.

(40) Trimarchi, G.; Binggeli, N. *Phys. Rev. B* **2005**, *71*, 035101.

(41) Yang, S. Q.; Zhang, T. R.; Tao, Z. L.; Chen, J. *Acta Chim. Sinica* **2013**, *71*, 1029.

(42) Varela, A.; Dios, S.; Parras, M.; Hernando, M.; Fernández-Díaz, M. T.; Landa-Cánovas, A. R.; González-Calbet, J. M. *J. Am. Chem. Soc.* **2009**, *131*, 8660.

(43) David, A. M.; Naoyukl, N.; Akira, O.; John, L. G.; Harold, Y. H. *Nature* **2004**, *430*, 657.

(44) Pullar, R. C.; Penn, S. J.; Wang, X. R.; Reaney, I. M.; Alford, N. M. *J. Eur. Ceram. Soc.* **2009**, *29*, 419.

(45) Toupin, M.; Brousse, T.; Bèlanger, D. *Chem. Mater.* **2004**, *16*, 3184.

(46) Zhang, S. L.; Livi, K. J. T.; Gaillot, A. C.; Stone, A. T.; Veblen, D. R. *Am. Mineral.* **2010**, *95*, 1741.

(47) Schmid, H. K.; Mader, W. *Micron* **2006**, *37*, 426.

(48) Gorlin, Y.; Lassalle-Kaiser, B.; Benck, J. D.; Gul, S.; Webb, S. M.; Yachandra, V. K.; Yano, J.; Jaramillo, T. F. *J. Am. Chem. Soc.* **2013**, *135*, 8525.

(49) Takashima, T.; Hashimoto, K.; Nakamura, R. *J. Am. Chem. Soc.* **2012**, *134*, 18153.

(50) Hubert, A. G.; Shyam, S. K.; Bhaskar, S.; Frederick, T. W. *Appl. Catal. B: Environ.* **2005**, *56*, 9.

(51) Trotochaud, L.; Samantha, L.; Ranney, J. K.; Boettcher, S. W. *J. Am. Chem. Soc.* **2014**, *136*, 6744.

(52) Stoerzinger, K. A.; Risch, M.; Suntivich, J.; Lü, W. M.; Zhou, J.; Biegalski, M. D.; Christen, H. M.; Venkatesan, T.; Shao-Horn, Y. *Energy Environ. Sci.* **2013**, *6*, 1582.

(53) Liu, H. J.; Li, J.; Xu, X. H.; Wang, F.; Liu, J. J.; Li, Z. L.; Ji, J. *Electrochim. Acta* **2013**, *93*, 25.

(54) Briático, J.; Alascio, B.; Allub, R.; Butera, A.; Caneiro, A.; Causa, M. T.; Tovar, M. *Phys. Rev. B* **1996**, *53*, 14020.

(55) Su, H. Y.; Gorlin, Y.; Man, I. C.; Calle-Vallejo, F.; Nørskov, J. K.; Jaramillo, T. F.; Rossmeisl, J. *Phys. Chem. Chem. Phys.* **2012**, *14*, 14010.

(56) Cheng, F. Y.; Zhang, T. R.; Zhang, Y.; Du, J.; Han, X. P.; Chen, J. *Angew. Chem., Int. Ed.* **2013**, *52*, 2474.

(57) Choi, Y.; Lin, M. C.; Liu, M. L. *Angew. Chem., Int. Ed.* **2007**, *46*, 7214.

(58) Loshkareva, N. N.; Nomerovannaya, L. V.; Mostovshchikova, E. V.; Makhnev, A. A.; Sukhorukov, Y. P.; Solin, N. I.; Arbuzova, T. I.; Naumov, S. V.; Kostromitina, N. V. *Phys. Rev. B* **2004**, *70*, 224406.

(59) Coey, J. M. D.; Venkatesan, M. *J. Appl. Phys.* **2002**, *91*, 8345.